UCRL-JC-133645
PREPRINT

Low-defect reflective mask blanks for Extreme Ultraviolet Lithography

S. C. Burkhart
C. Cerjan
P. Kearney
P. Mirkarimi
C. Walton
A. Ray-Chaudhuri

This paper was prepared for submittal to the
Society of Photo-Optical Instrumentation Engineers
24th Annual International Symposium of Microlithography
Santa Clara, CA
March 14-19, 1999

March 11, 1999

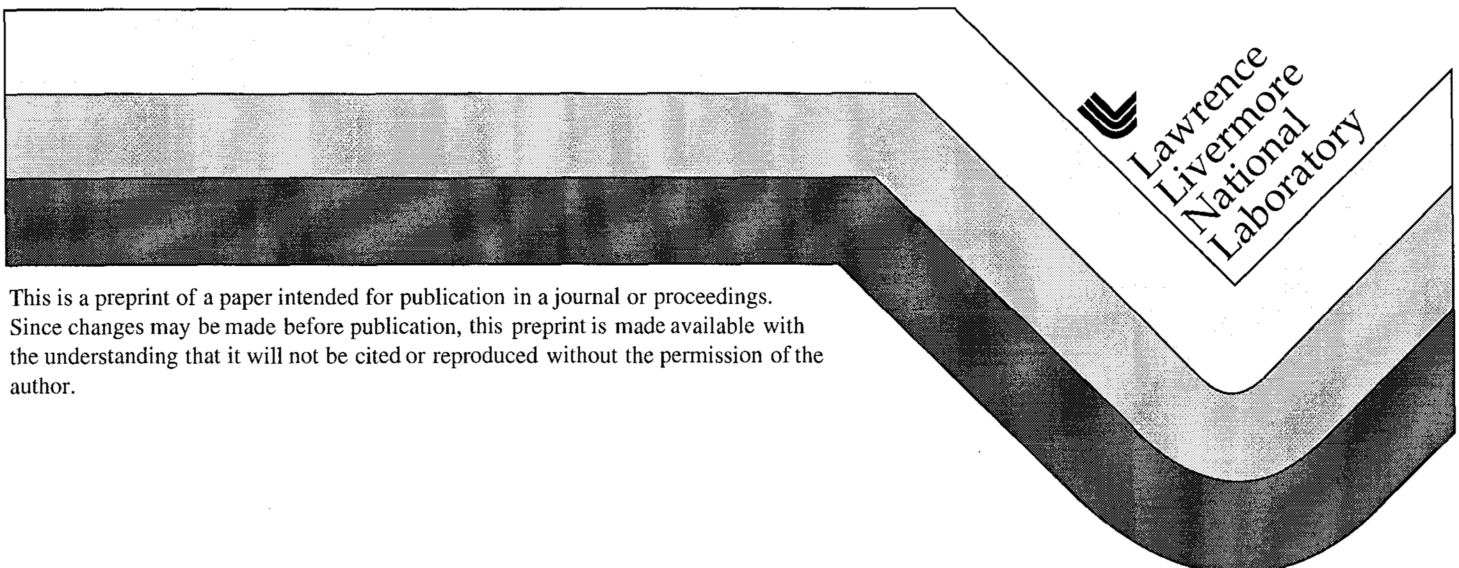

This is a preprint of a paper intended for publication in a journal or proceedings. Since changes may be made before publication, this preprint is made available with the understanding that it will not be cited or reproduced without the permission of the author.

DISCLAIMER

This document was prepared as an account of work sponsored by an agency of the United States Government. Neither the United States Government nor the University of California nor any of their employees, makes any warranty, express or implied, or assumes any legal liability or responsibility for the accuracy, completeness, or usefulness of any information, apparatus, product, or process disclosed, or represents that its use would not infringe privately owned rights. Reference herein to any specific commercial products, process, or service by trade name, trademark, manufacturer, or otherwise, does not necessarily constitute or imply its endorsement, recommendation, or favoring by the United States Government or the University of California. The views and opinions of authors expressed herein do not necessarily state or reflect those of the United States Government or the University of California, and shall not be used for advertising or product endorsement purposes.

Low-defect reflective mask blanks for Extreme Ultraviolet Lithography

Scott Burkhart, Charles Cerjan, Pat Kearney, Paul Mirkarimi, Christopher Walton (*Lawrence Livermore National Laboratory, Livermore, CA 94550*), Avi Ray-Chaudhuri (*Sandia National Laboratories, Livermore, CA 94550)*

ABSTRACT

Extreme Ultraviolet Lithography (EUVL) is an emerging technology[1] for fabrication of sub-100 nm feature sizes on silicon, following the SIA roadmap well into the 21st century. The specific EUVL system described is a scanned, projection lithography system with a 4:1 reduction, using a laser plasma EUV source. The mask and all of the system optics are reflective, multilayer mirrors which function in the extreme ultraviolet at 13.4 nm wavelength. Since the masks are imaged to the wafer exposure plane, mask defects greater than 80% of the exposure plane CD (for 4:1 reduction) will in many cases render the mask useless, whereas intervening optics can have defects which are not a printing problem. For the 100 nm node, we must reduce defects to less than 0.01/cm^2 @80nm or larger to obtain acceptable mask production yields. We have succeeded in reducing the defects to less than 0.1/cm^2 for defects larger than 130 nm detected by visible light inspection tools, however our program goal is to achieve 0.01/cm^2 in the near future. More importantly though, we plan to have a detailed understanding of defect origination and the effect on multilayer growth in order to mitigate defects below the 10^{-2}/cm^2 level on the next generation of mask blank deposition systems. In this paper we will discuss issues and results from the ion-beam multilayer deposition tool, details of the defect detection and characterization facility, and progress on defect printability modeling.

Keywords: EUVL, EUV Lithography, masks, multilayer, defects

1. INTRODUCTION

1.1. Mask blank fabrication

EUVL mask blanks are fabricated in a class 100 facility at Lawrence Livermore National Laboratory (LLNL), which has been described previously in detail,[2,3] and is summarized here for completeness. The facility resides in the LLNL Microfabrication Facility, which contains the needed support infrastructure including utilities and cleanrooms. The mask blanks are currently fabricated by depositing 40–60 layer pairs of molybdenum and silicon with a period of ~6.8 nm on a silicon substrate. Mo and Si were chosen because they are the best characterized, and can be wavelength matched to the other Mo-Si coated optics in the prototype projection system.[4] The Si substrates are specially cleaned but are otherwise standard epi Si 150 mm wafers, which can be obtained with defect-densities below 0.05 defects/cm^2. Processing begins when the wafers are unloaded from their shipping containers and put into SMIF pod clean enclosures in a class 1 auxiliary loading unit, then inspected for defects in a visible light scattering inspection tool. The bare substrates (wafers) are inspected for light point defects down to an equivalent polystyrene latex sphere size of 80 nm. From there they are inserted into the Low Defect Deposition (LDD) tool (Fig. 1) for multilayer deposition.

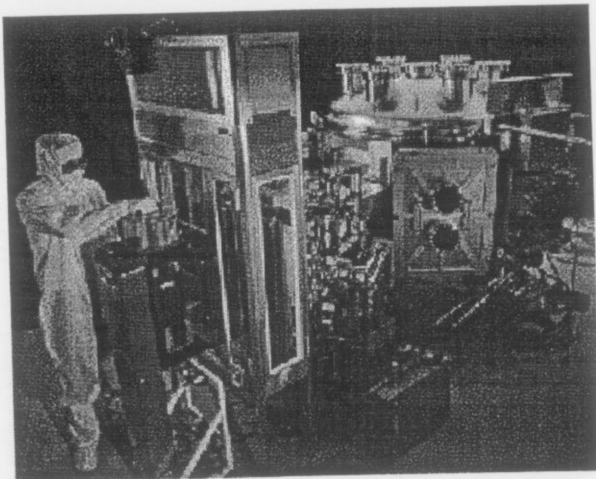

Fig. 1. Photograph of the low-defect deposition facility at LLNL. Mask substrates are inserted using SMIF technology, and coated automatically following a deposition system script.

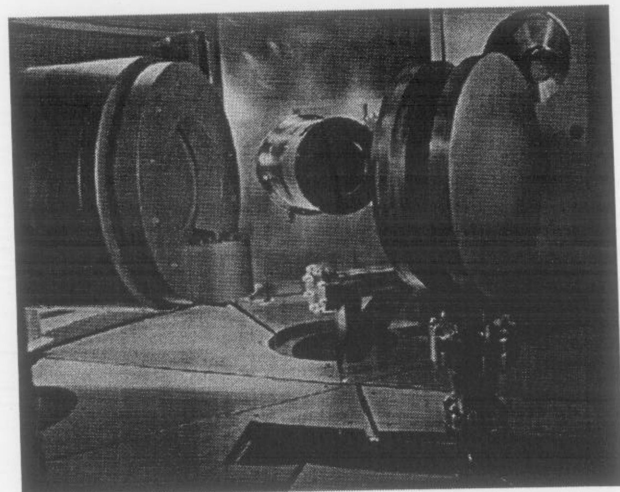

Fig. 2. Internal view of the deposition chamber showing the ion-gun (left) and the rotatable Mo/Si target. The substrate chuck is shown in the background, although it has recently been upgraded to an electrostatic chuck.

The SMIF pod is mounted on the cassette elevator, lowered and inserted into the load-lock chamber of the LDD which is evacuated separately from the robot and deposition chamber. Each substrate in turn is robotically collected through a slit valve and transferred onto the electrostatic deposition chuck through another slit valve, and deposition commences. Deposition parameters can be varied for each substrate according to a procedural script that controls deposition time, substrate rotation speed, ion-gun voltage and current, and sputtering target angle. The sputtering target (Fig. 2) consists of a disk of silicon and one of molybdenum mounted to a rotatable, water-cooled holder. The process flow is shown in Fig. 3. Following substrate preparation and defect characterization, the multilayers are coated sequentially until the requisite number of layer pairs are deposited (usually 40). Prior to unloading, the coated substrate (mask blank) is allowed to cool and discharge for a short period of time, then rotated into position for access by the robot.

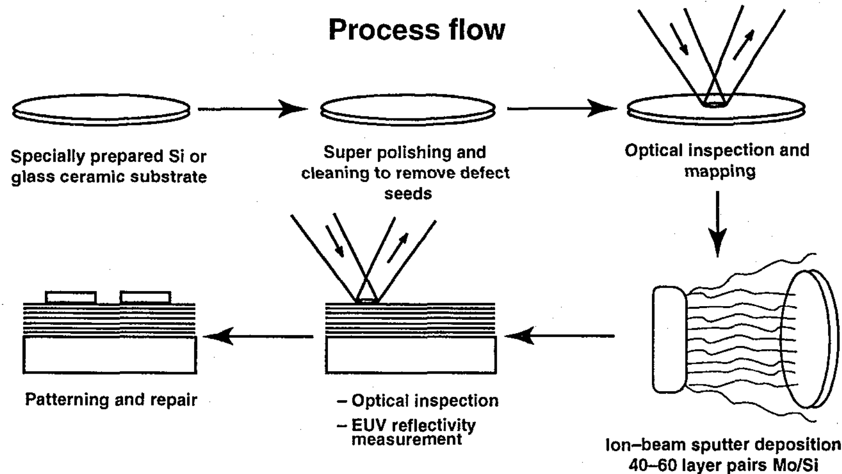

Fig. 3. Process flow for mask blank fabrication begins with substrate preparation and characterization. The mask substrates are then multilayer coated, and further analyzed prior to patterning.

The mask blank is removed from the chuck and returned to the cassette in the load-lock chamber. This process continues until all the substrates are coated. Following deposition, the mask blanks are scanned again by the visible-light scattering tools, and a select few are analyzed in more detail by atomic-force microscope, SEM and probed for defect composition using the EDS feature of the SEM. Finally, selected samples of the mask blanks are characterized for reflectivity at EUV as described in the next section.

1.2. Performance characterization

Defects aside, the most important characteristic of the mask blank is high reflectivity uniformly over the imaged part of the mask blank. For the prototype EDS projection EUVL system, the mask pattern is placed on a rectangle sized 96mm X 130mm with a reflectance of >65% and a uniformity of ±1% over the patterned area. Reflectance qualification is performed at the Advanced Light Source at Lawrence Berkeley National Laboratory.[5] We have achieved reflectivities up to 67% with 60 layer pairs.[2,3]

1.3. Defect characterization

The goal of defect characterization is two-fold: first, to detect defects on the blank at the smallest size possible, in order to provide blanks of a known quality level for printing; and second, to characterize each defect well enough to learn its source, in order to guide process improvements that will reduce the number of defects. These goals can be approached by the same methods that we will describe here.

Our primary detection tool is a commercial optical inspection tool, which spins the wafer and scans the surface with a focused laser probe at λ = 488nm. Defects are detected by the light they scatter into several large detectors. The inspection tool records defect sizes and locations in an output file, which functions as a defect map of the substrate. This map is in a ".tff" file format originated by KLA/Tencor, Inc. which is readable by many characterization tools.

The defect map contains no information about the nature of the defect except the scattered intensity, in parts per million (ppm) of the incident intensity. The scattered intensity depends on the scattering cross-section (C_{sc}) of the defect, which in turn depends on its size, composition and shape, and on the roughness and reflectivity of the surface on which the defect rests, and on the incident wavelength and angle. For a spherical particle of known composition, the cross-section can be calculated according to standard scattering theory (Rayleigh scattering for small particles of diameter $d \ll \lambda$; Mie scattering for $d \approx \lambda$). The cross section can also be tested experimentally by comparison with scattering from standard latex spheres, which are available commercially at tightly specified diameters. These models and experiments are useful for calibrating the inspection tool, and for giving particle sizes in latex equivalents, but they do not give a measurement of the true particle size when the composition is unknown.

To obtain more information on the defects, the defect map is used to locate and characterize individual defects by atomic-force microscopy (AFM) and scanning electron microscopy (SEM) (Fig. 4). The AFM can give accurate physical dimensions of a defect, and the SEM can give complete morphology (including recessed areas inaccessible to the AFM tip), and chemical composition by energy-dispersive spectroscopy (EDS) of the characteristic x-rays emitted under the bombardment of the electron beam. Results from these techniques on typical defects will be presented below.

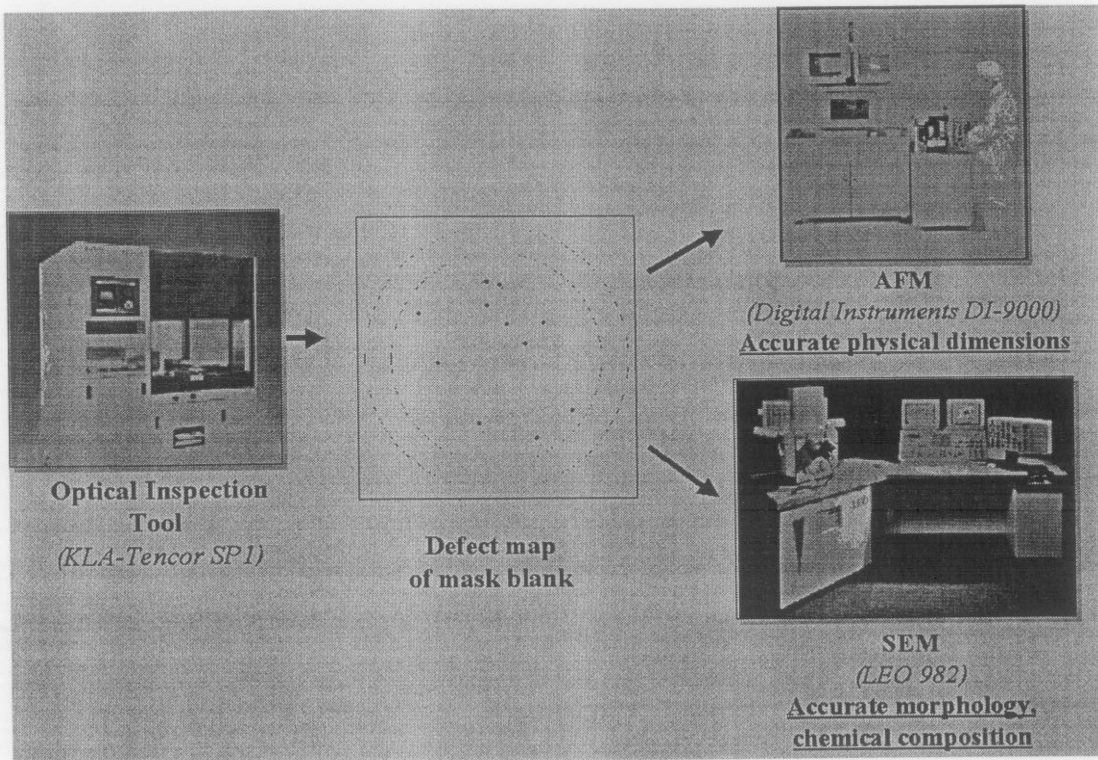

Fig. 4. Schematic of detection and characterization scheme: primary detection by optical scanning maps defects for further characterization by AFM, SEM.

In practice this cross-registration of the same defect from tool to tool has difficulties. Because the optical inspection tool is intended as a high-throughput commercial device, there are inaccuracies of 25-100μm in measuring the defect locations. These result both from difficulties in defining a reproducible reference frame on a featureless bare wafer, and from errors in recording the position of the wafer over time as defects are found. The maximum scan sizes on the AFM and SEM which would detect a 100nm defect are about 20μm square, so multiple scans are required to locate each defect. Solutions to these problems include systematic logging of position errors over time and location on the wafer, and subtracting them out with a spline fit, and adding known registration marks to the wafers, which can then establish a common coordinate system for all tools.

By current models, the smallest "killer" defects that would cause unacceptable CD changes at printing are 50-70nm, depending whether the defect is an absorber or a phase error. The smallest particle size the inspection tool can detect depends on the roughness of the blank. In general, the Mo/Si multilayer is slightly rougher than the bare wafer. With the current inspection tool the detection limit is approximately 80nm (latex equivalent) on a bare wafer and 80-100nm on a coated wafer. These sizes correspond to about 57nm and 57-71nm in Mo or Si spheres, because of the higher refractive indices. Tool improvements in cooperation with manufacturers are expected to decrease these detection limits.

2. MASK BLANK DEFECTS

2.1. Introduction to defect classes

Multilayer mask blank coating defects are broadly divided into phase defects and amplitude defects (Fig. 5). A phase defect is a location where an abrupt phase change at the mask is projected to the areal image as an unexposed area at the projected defect boundary, due to the limited spatial frequency bandpass of the projection optics. Amplitude defects are further divided into critical (>80 nm) defects or contamination, and sub-critical defect sizes or else intrinsic multilayer roughness which may

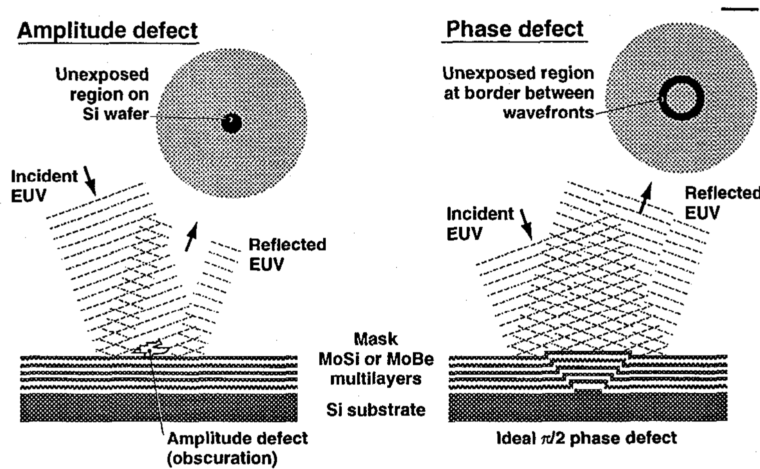

Fig. 5. An amplitude defect is an obscuration of the illuminating beam (like mask pattern absorber), whereas a phase defect is a growth discontinuity or replicated substrate discontinuity which leads to an abrupt phase shift and if resolved, a printing defect.

be decorated up to critical size by the multilayer coating process. The larger defects we refer to as extrinsic defects, whereas the smaller ones are called either intrinsic defects or sub-critical defects. In the following sections, we discuss these two classes.

2.2. Extrinsic defects

The path to defect elimination depends on the source of the defects. For environmental particles, good cleanroom practices combined with clean handling procedures and equipment such as SMIF and robotics are essential. To reduce defects due to flaking during deposition, one must utilize special shield materials and surface preparation to reduce the likelihood of flaking, and use appropriate system geometries so that any flaking that does occur will likely not impact yields.

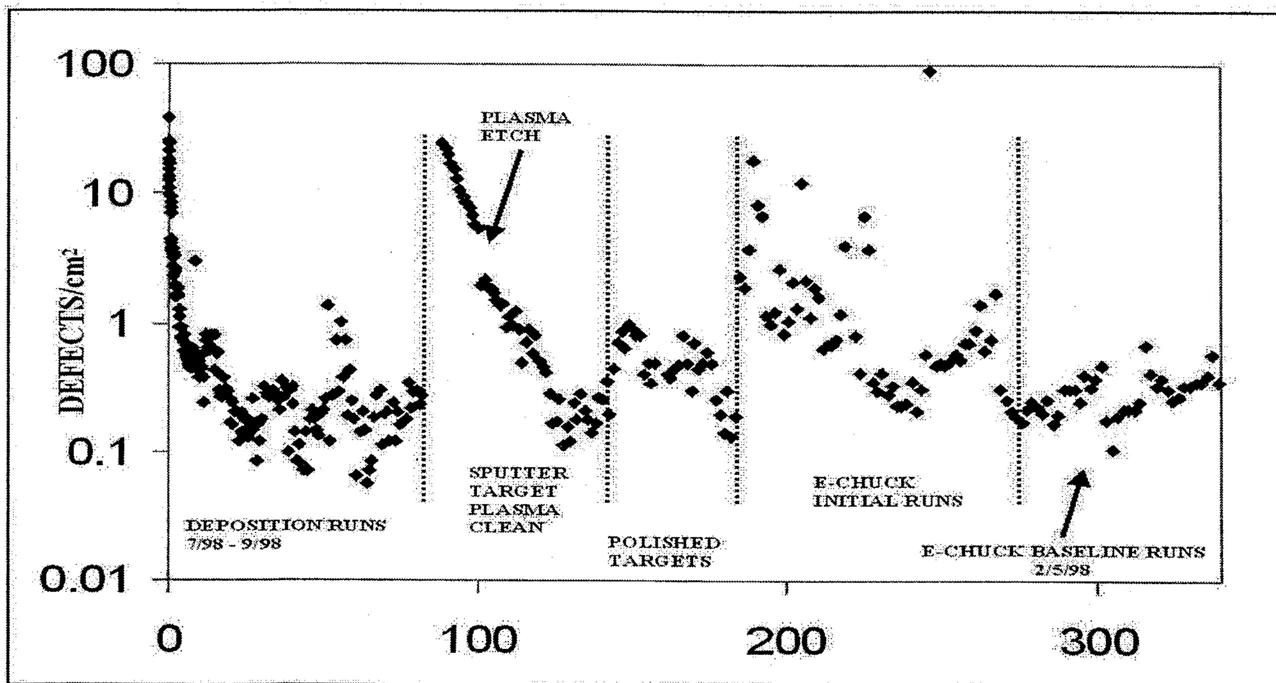

Fig. 6. Defect counts observed during nine months of operation. The original defect count problem has been corrected using polished Si sputtering targets, and more recently the variability of defect counts has been much improved using an electrostatic chuck.

The reduction of defects due to material ejected from the source requires a well designed ion source to minimize particle generation, clean, well controlled target surfaces, and a system geometry designed to minimize the impact of the remaining particles on yield. Eliminating flux nucleation of particles requires the use of pure chemicals, good vacuum practices, and the elimination/engineering of plasma sheaths in the high flux regions.

Defect levels for each sample during our target defect experiments are plotted in Fig. 6. We found that after changing targets defect levels were very high; it took many runs for the system to clean up. We suspected surface contamination on the targets was causing the defects. The first method we tried to clean the targets was defocusing the ion beam to sputter clean the targets. The experiment consisted of repeatedly growing several blanks followed by sputter cleaning the target. Although the sputter-cleaned target started out an order of magnitude dirtier than the uncleaned target, it achieved baseline defect levels more quickly. The large discontinuities in the curve occur whenever we sputter cleaned the target. Next we tried polishing the targets to remove the bulk of surface damage. The data show that polished targets were able to get to baseline defect levels almost immediately, without using nearly as much target as the sputter cleaning method.

Another potential source of defects is the mechanism used to hold the wafer. We switched from a mechanical clamping mechanism to an electrostatic chuck to eliminate particles from mechanical motions and front surface contact on the blank. The electrostatic chuck was better shielded from the depositing flux, and all moving parts were far from the front surface of the wafer. This has improved the repeatability of our defect experiments ie. there has been less scatter in the added defect counts for deposition runs which use the electrostatic chuck. However, the mean added defect density has not improved.

Our ability to cross register defect locations between our light scattering tool and our AFM and SEM allows us to begin to observe individual defects with the SEM/AFM. Two common defect morphologies are shown in Figs. 7(a) and 7(b). Figure 7(a) shows a SEM of a roughly spherical particle a few microns in size. The spherical particle shape is certainly suggestive of vapor phase nucleation and growth.[7] EDS shows only molybdenum and silicon in the particle. Figure 7(b) shows a SEM of an irregular particle that is approximately one micron in size. It seems to be made up of several semi-spherical segments of diameter ~250nm. EDS of the irregular particle (Fig. 8) shows traces of Fe and Cr (possibly stainless steel) at its core. With the shape and chemical information these techniques provide, we hope to be able to trace the particles back to their source and eliminate them.

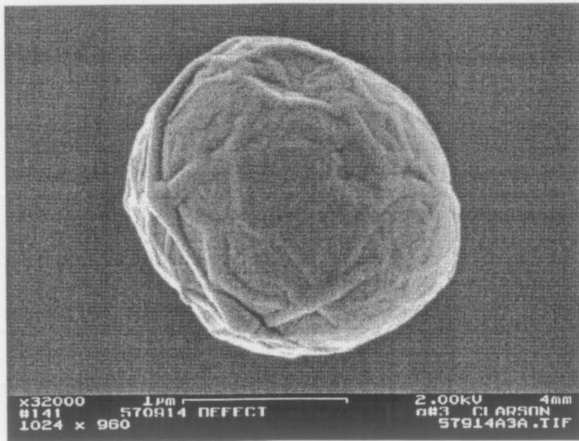

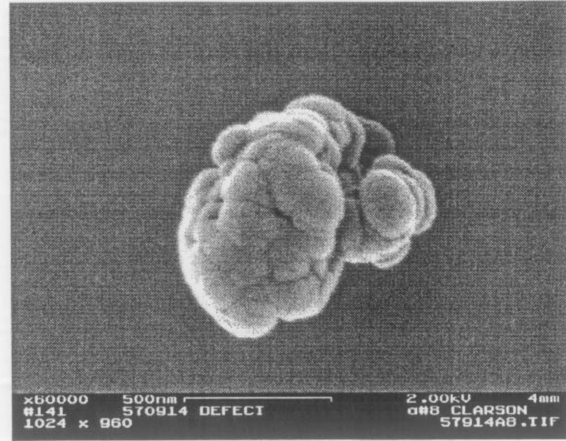

Fig. 7(a) SEM of a roughly spherical defect found on a mask blank.

Fig. 7(b). SEM of a frequently seen irregular defect on a mask blank.

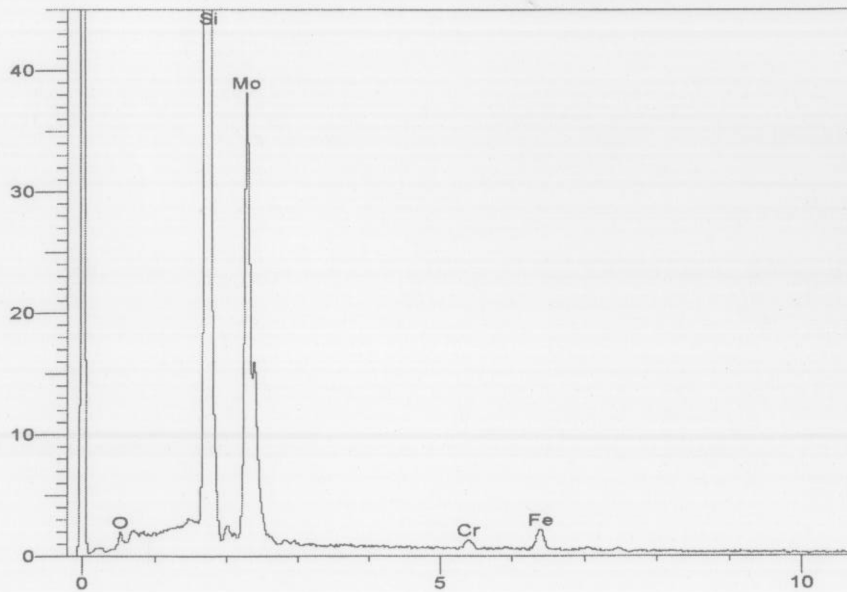

Fig. 8. EDS spectra of the defect in Fig. 7(b) showing Fe and Cr covered with Mo and Si.

2.3. Intrinsic and sub-critical defects

As noted earlier, the reticles used for EUV lithography depend on a Mo/Si multilayer coating to reflect light into the imaging system. Thus, there is the potential for (i) defects due to the multilayer growth process, which we shall term intrinsic defects, and (ii) sub-critical defects (particulates, pits, etc.) on the substrate or in the multilayer in which the topology of the defect is replicated or amplified during multilayer growth. Sub-critical defects are expected to be replicated in the topology of the multilayer if the deposition flux is perfectly uniform at every point on the substrate surface; however, if there is shadowing there can be variations in the deposition rate near the defect. This has the potential to induce a small, nonprintable sub-

critical defect to be amplified into a printable, critical defect by the multilayer growth process. Shadowing will be a function of the geometry of the deposition flux relative to the substrate and the defect topology, and in general is expected to become more significant as the angle of incidence between the deposition flux and substrate is decreased from normal incidence.

The nature of these defects is such that the lateral size (in the plane of the film) could be significantly larger than the topography change at the surface of the multilayer coating. Conventional (visible) light scattering methods, which rely on changes in surface topography, would not be expected to detect such defects. However, scattering methods that use EUV light do have the potential to detect these defects, and progress has been made in detecting defects with EUV scattering techniques.[9] In order to investigate if defect amplification occurs in our deposition process, experiments are planned in which standard Si wafers will be decorated with a sufficient density of sub-critical defects of known sizes (5-50nm), and subsequently coated with a Mo/Si multilayer film. The samples will then be characterized using techniques such as transmission electron microscopy, atomic force microscopy, and EUV scattering. With the machinery in place to controllably introduce these very small defects and characterize their effects, it should be straightforward to investigate the effects of process parameters on defect amplification, which could then be used to minimize this effect if needed.

2.4. Defect printability studies

Given the significant difficulties of detecting and characterizing small defect features, numerical simulations are being employed to augment the ongoing experimental effort. Although a complete, three-dimensional parametric study would be prohibitive, it is expected that the dominant scattering effects will be identified to provide guidance for the experimental investigations. Our primary means of addressing this problem is the Finite Difference Time Domain (FDTD) algorithm as implemented in a LLNL simulation program (TSAR) and in the more commonly known modeling program TEMPEST.[9] Models of amplitude and phase defects are being applied to determine not only the minimum critical defect size, but the effect of defects buried within the multilayer stack.

To obtain initial learning on the printability of phase defects, a study was performed utilizing the 10x Microstepper at Sandia National Laboratories. A multilayer mask with programmed isolated defects was prepared by etching pits 44 nm deep (13.1 Pi phase) into the substrate prior to depositing a multilayer coating ~250nm thick. AFM measurements were performed to verify the amount of material removed as well as to confirm that the sidewall angle of the pit was greater than 88°. Aerial image simulations using Prolith/3D were performed to predict the printability of these phase defect features. A simple resist threshold model was utilized with the threshold set at a level required to simultaneously print 100 nm dense lines. Camera wavefront aberrations as measured by EUV interferometry were incorporated into the simulation. The RMS wavefront error was 0.05 waves at a wavelength of 13.4 nm. Figure 9 shows the top-down view of the threshold aerial image for a series of defects ranging in width from 0.2μm – 1.1 μm and length of 2.0 μm on the mask (10x). Simulation predicts that the larger features will only print at the edges where there is a phase discontinuity. The asymmetry in the features is due to camera aberrations that become evident at low-K_1 printing.

During the actual print test, however, none of these features printed within a 1μm depth of focus and 10% dose window. This result suggests that the simulation was overly conservative in assuming that an abrupt phase discontinuity exists at the feature edges. Another conservative assumption was made when using a resist threshold model. Both experimental and theoretical study is in progress to understand the multilayer growth and the degree of conformity that one can expect. This initial work suggests that it may be quite difficult to produce a deleterious phase defect in the multilayer.

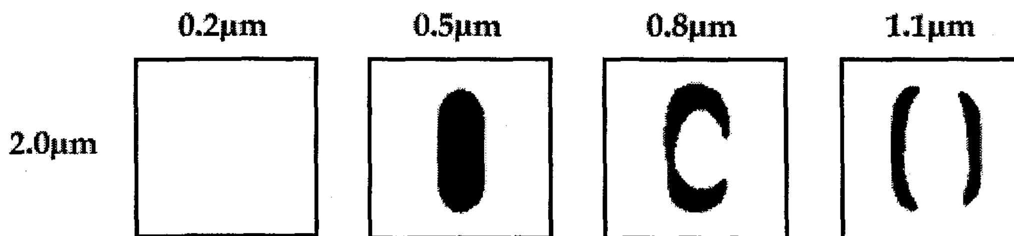

Fig. 9 Prolith/3D predictions for printability of ideal 13.1π phase defect 'pits' using measured 10X camera performance. The defect size on the mask was 2.0 μm X 0.2 – 1.1 μm.

3. CONCLUSIONS

Defect reduction on EUVL mask blanks is proceeding by parallel efforts on deposition contamination control, experiments on understanding multilayer growth science, defect detection and characterization, and printability modeling. Technological advances are being made in characterization and in our understanding of defect growth in thin films and that will ultimately result in identification of the primary causes of the defects. Finally, we anticipate being able to use this knowledge to significantly reduce the defects using present and future multilayer deposition tools.

4. ACKNOWLEDGMENTS

This work was performed under the auspices of the U. S. Department of Energy by the Lawrence Livermore National Laboratory under Contract No. W-7405-ENG-48. Funding was provided by the Extreme Ultraviolet Limited Liability Company (EUV LLC) to Lawrence Livermore National Laboratory and Sandia National Laboratories under a Cooperative Research and Development Agreement. The portion of this work, performed at Sandia National Laboratories, is supported by the Extreme Ultraviolet Limited Liability Company (EUV LLC) and by the U. S. Department of Energy under contract DE-AC04-94AL85000. Additional acknowledgment goes to International SEMATECH, who provided funding for major portions of this work.

5. REFERENCES

1. C. Gwyn, R. Stulen, D. Sweeney, and D. Attwood, "Extreme ultraviolet lithography," *J.Vac. Sci. Technology B,* 16: (6) 3142-3149 Nov/Dec 1998
2. S. P. Vernon, P. A. Kearney, W.M. Tong, S. Prisbrey, C. Larson, C. E. Moore, F. W. Weber, G. Cardinale, P. Y. Yan, S. D. Hector, "Masks for extreme ultraviolet lithography," in *18'th Annual BACUS Symposium on Photomask Technology and Management,* Brian J. Grenon, Frank E. Abboud, Editors, Proceedings of SPIE Vol. 3546, pp 184-193 (1998)
3. M. Bujak, S. Burkhart, C. Cerjan, P. Kearney, C. Moore, S. Prisbrey, D. Sweeney, W. Tong, S. Vernon, C. Walton, A. Warrick, F. Weber, M. Wedowski, K. Wilhelmsen, in *16'th Annual Symposium on Mask Technology for Integrated Circuits and Micro-Components '98,* Dr. Uwe Behringer, Editor, GMM-Fachbericht; 25, pp.39-48 (1998)
4. D. Sweeney, R. Hudyma, H. Chapman, and D. Schafer, "EUV optical design for a 100 nm CD imaging system," *Emerging Lithographic Technologies II,* Y. Vladimirsky, ed., SPIE Proceedings, vol. 3331, 2-10, 1998.
5. J. H. Underwood and E. M. Gullikson, "Beamline for measurement and characterization of multilayer optics for EUV lithography," *Emerging Lithographic Technologies II,* Y. Vladimirsky, ed., SPIE Proceedings, vol. 3331, 52-61, 1998.
6. D. G. Stearns, D. P. Gaines, D. W. Sweeney, "Nonspecular X-ray scattering in a multilayer-coated imaging system," *J. Appl. Phys.* **84** (2), 1003-28 (1998).
7. G.S. Selwyn, J. Singh and R.S. Bennet, "In situ laser diagnostic studies of plasma-generated particulate contamination," *J. Vac. Sci. Technol.* A 7(4) 1989, 2758-2765.
8. S. Jeong, M. Idir, Y. Lin, L. Johnson, S. Rekawa, M. Jones, P. Denham, P. Batson, P. Kearney, E. Gullikson, J. H. Underwood, and J. Bokor, *J. Vac. Sci. Technol.* B 16, 3430 (1998).
9. A. Wong, *Rigorous Three-Dimensional Time-Domain Finite-Difference Electromagnetic Simulation* (Electronics Research Laboratory, University of California, Berkeley, 1994).